Earthquake nucleation characteristics revealed by seismicity response to seasonal stress variations induced by gas production at Groningen.

Mateo Acosta[1*], Jean-Philippe Avouac[1,2], Jonathan D. Smith[1], Krittanon Sirorattanakul[1], Hojjat Kaveh[1,2], Stephen J. Bourne[3]

[1]Division of Geological and Planetary Sciences (GPS), California Institute of Technology, Pasadena, CA, USA.

[2]Mechanical and Civil Engineering (MCE), California Institute of Technology, Pasadena, CA, USA.

[3]Shell Global Solutions, Amsterdam, NL.

*Corresponding author. Mateo Acosta: acosta@caltech.edu

Key Points:

- An improved reservoir, geomechanical, and seismicity modelling workflow for is proposed for forecasting induced seismicity at various timescales.
- Short-timescale stress variations allow constraining the characteristics of the earthquake nucleation process using Groningen as case study.
- Initial strength excess and finite duration of the nucleation process allow reproducing long-and-short timescale characteristics of seismicity.

Abstract

Deterministic earthquake prediction remains elusive, but time-dependent probabilistic seismicity forecasting seems within reach thanks to the development of physics-based models relating seismicity to stress changes. Difficulties include constraining the earthquake nucleation model and fault initial stress state. Here, we analyze induced earthquakes from the Groningen gas field, where production is strongly seasonal, and seismicity began 3 decades after production started. We use the seismicity response to stress variations to constrain the earthquake nucleation process and calibrate models for time-dependent forecasting of induced earthquakes. Remarkable agreements of modelled and observed seismicity are obtained when we consider (i) the initial strength excess, (ii) the finite duration of earthquake nucleation, and (iii) the seasonal variations of gas production. We propose a novel metrics to quantify the nucleation model's ability to capture the damped amplitude and the phase of the seismicity response to short-timescale (seasonal) stress variations which allows further tightening the model's parameters.

Plain Language Summary

Earthquakes are difficult to predict with certainty, but progress in forecasting their likelihood using probabilistic models based on stress changes has been made. However, challenges remain in understanding how earthquakes start and the initial conditions of faults. Here, we analyzed induced earthquakes in the Groningen gas field, where production is seasonal and seismic activity began much after gas production. By studying how the earthquakes respond to changes in stress, we could better understand how they start and develop models to forecast their temporal occurrence. By considering factors like the initial strength of the faults, the duration of earthquake initiation, and seasonal variations in gas production we could accurately match the observed seismic activity. We introduced a new measure to evaluate how well the models captured the dampened strength and timing of seismic activity in response to short-term stress changes (such as seasonal variations), which helped refine the model's parameters.

1 Introduction

Numerous activities related to the decarbonization, or security of energy production involve managing subsurface reservoirs (geothermal, CO_2 sequestration, hydrogen storage, conventional and unconventional oil-and-gas extraction). Induced earthquakes are a major obstacle to these activities (Candela et al., 2018; Ellsworth, 2013; Goebel & Brodsky, 2018; Grigoli et al., 2017; Kaven et al., 2015; Raleigh et al., 1976; Shirzaei et al., 2016; Walsh & Zoback, 2015; Zhai et al., 2019) raising the need for improved methods to forecast induced seismicity. The modern understanding that earthquakes result from unstable frictional fault slip (Scholz, 2019) provides a foundation to forecast changes of earthquake rate in response to stress changes, ΔS (Bourne et al., 2018; Bourne & Oates, 2017b; Dahm & Hainzl, 2022; Dempsey & Suckale, 2017; King et al., 1994; Kühn et al., 2022; Langenbruch et al., 2018; Richter et al., 2020; Zhai et al., 2019). The approach requires a model of earthquake nucleation and knowledge of the stress change needed to initiate it (strength excess). At its simplest, the standard Coulomb friction model, CF, assumes that unstable fault slip initiates instantaneously when the ratio of shear stress to effective normal stress exceeds the static friction coefficient. In this context, the often-observed lagged response of the seismicity to stress changes can be modeled through an initial strength excess (Bourne & Oates, 2017b). While the CF approach has been found satisfying in several case studies (Bourne et al., 2018; Bourne & Oates, 2017b; Dempsey &

Suckale, 2017; Smith et al., 2022), this model neglects that earthquake nucleation might not be instantaneous, as evidenced by laboratory experiments (Dieterich, 1994) and the weak correlation of earthquakes with solid Earth tides (Beeler & Lockner, 2003; Cochran et al., 2004). Some models have introduced an *ad-hoc* critical time-to-failure (Dahm & Hainzl, 2022; Zhai et al., 2019) to account for either the initial strength excess or non-instantaneous nucleation. A more physical way to account for the finite duration of the nucleation process consists in assuming that nucleation is governed by rate-and-state friction, RS, (Dieterich, 1994), a model adopted with success in a number of studies (Candela et al., 2019; Langenbruch et al., 2018; Richter et al., 2020; Zhai et al., 2019). Discriminating between the CF and RS models has however proven elusive (Dempsey & Suckale, 2023) due to the lack of observational constraints on the nucleation process, and the eventual trade-off between the initial strength excess and the nucleation time. The CF and RS models yield very different forecasts if stress changes occur at short timescales compared to the characteristic time of the nucleation process(Heimisson et al., 2022), and the nucleation process might therefore be revealed from the seismicity response to large amplitude, short-timescale stress variations (Ader et al., 2014). Here we demonstrate that the nucleation process is not instantaneous and derive constraints on its characteristic timescales, fault friction parameters, and the initial strength excess by studying seismicity induced by gas extraction from the Groningen field, where strong seasonal variations of gas production (Figure.1A,B) generated significant seasonal seismicity variations.

The Groningen gas field in northeastern Netherlands (Figure.1A) is an ideal example to study induced seismicity due to well-known reservoir properties (Burkitov et al., 2016; de Jager & Visser, 2017; Oates et al., 2022), detailed seismicity catalog (Dost et al., 2017; Dost & Kraaijpoel, 2013; Smith et al., 2020; Willacy et al., 2018), and well-resolved surface subsidence (Smith et al., 2019; van Thienen-Visser & Breunese, 2015). Together, these data have allowed for calibration of models used to hindcast and forecast induced seismicity (Bourne et al., 2014, 2018; Bourne & Oates, 2017b; Buijze et al., 2017; Candela et al., 2019; Dahm & Hainzl, 2022; Dempsey & Suckale, 2017; E. R. Heimisson et al., 2022; Kühn et al., 2022; Meyer et al., 2022; Richter et al., 2020; Van Wees et al., 2017). Gas is extracted from a thin, laterally extensive (~100-300 m thickness for ~30*50 km horizontal dimension), porous and permeable (~15-20% porosity, ~3.55E-13 m^2 permeability (de Jager & Visser, 2017; Meyer et al., 2022)) reservoir hosted in the Rotliegend sandstone formation (Figure.1A,B). Production started in 1963 but earthquakes were not detected until 1991. Initially, the seismicity rate increased exponentially, despite steady annual extraction rates (Figure.1B, green curve). The 2012 M_w3.6 Huizinge earthquake, the largest event to date, caused public concern and a decision to decrease first and then shut-down production long before exhaustion of the gas reserve (Figure.1A,B, (Candela et al., 2018; Dost & Kraaijpoel, 2013)). More details about the gas field and the available data are given in Supplementary Item 1.

The various stress-based models developed so far consider either instantaneous seismicity nucleation with an initial strength excess (Bourne et al., 2018; Bourne & Oates, 2017b; Dempsey & Suckale, 2017, 2023; Meyer et al., 2022; Smith et al., 2022), a delayed response due to the nucleation process (Candela et al., 2019; Dahm & Hainzl, 2022; Kühn et al., 2022; Richter et al., 2020), or a combination of both (Dahm & Hainzl, 2022; R. Heimisson et al., 2021). These models fit well the observed seismicity based on yearly averaged stress changes, but predict drastically different responses to rapid variations of production such as shut-ins (E. R. Heimisson et al., 2022; Meyer et al., 2022). Moreover, a bias could be introduced as these models were

calibrated ignoring that, in reality, gas extractions show ~60-80% larger production in the winter from 1975 to 2013 (Figure.1B). Ignoring short-timescale, large-amplitude stress variations could bias the model because the seismicity response to stress changes is non-linear: the CF is non-linear through the initial strength excess and Kaiser effect (seismicity rate drops to zero when the Coulomb stress is lower than previous peak values); the RS includes a delayed Kaiser effect and, adding further non-linearity, an exponential dependence on ΔS (E. R. Heimisson & Segall, 2018). The introduction of a stress threshold, if an initial strength excess is allowed, is another source of non-linearity. Hereafter, we compare models with or without account for seasonal stress variations to illuminate the characteristics of the nucleation process.

2 Materials and Methods

We present a summary of the modelling strategy (Figure.S1) that allows us to resolve (i) the pore pressure diffusion due to injection/extraction from a porous reservoir, (ii) the mechanical response of the reservoir to pressure variations, and (iii) the relation between stress changes and seismicity adopted in this study. Finally, we present the fundamentals of other analysis techniques used such as the synthetic catalog generation, the Schuster test, and the metric to quantify seasonality in synthetic catalogs.

2.1 Modelling workflow

Our modeling workflow (Figure. S1) consists of different modules which allow us to predict reservoir pressure, stress changes within and outside the reservoir, subsidence and seismicity based on the flow rates at the wells. The parameters for the different modules are optimized from matching the observations (well pressure, subsidence, seismicity).

2.1.1 From fluid extraction to pressure changes.

To relate fluid extraction to pressure changes in the reservoir, we use a simplified reservoir model (Meyer et al., 2022) which assumes vertical flow equilibrium (VFE) to compute fluid pressure diffusion in the reservoir from the extraction history. This model assumes that the timescale for vertical pressure equilibrium is much shorter than the horizontal one due to the thin and elongated geometry of the reservoir. The problem becomes a 2-dimensional one and we solve the combined conservation of momentum and Darcy's law using the open-source finite element library FEniCS (Logg et al., 2012) and calibrate the model's parameters by history matching the well pressure time-histories. By reducing the computation cost using the VFE assumption, we can generate pressure ($\Delta \mathrm{p}(\mathrm{x}, \mathrm{y}, \mathrm{t})$) space-time histories in the Groningen reservoir with 1-month temporal discretization, allowing us to quantify the effect of seasonal variations of extraction in the pressure field (See Supplementary Item 2.1 for details).

2.1.2 From pressure changes to reservoir deformation and stress changes.

We use the poroelastic mechanical model from Smith et al. (Smith et al., 2022) to relate the fluid pressure changes to stress changes within and outside the reservoir.

$\Delta \mathrm{p}(\mathrm{x}, \mathrm{y}, \mathrm{t})$ calculated using the VFE reservoir model (section 2.2.1) is combined with the geodetically derived uniaxial compressibility ($C_m(x, y)$;(Smith et al., 2019)), and the reservoir thickness ($h(x, y)$) such that the reservoir compaction writes:

$$C = C_m(\mathrm{x}, \mathrm{y}). \Delta \mathrm{p}(\mathrm{x}, \mathrm{y}, \mathrm{t}). \mathrm{h}(\mathrm{x}, \mathrm{y}) \qquad (1)$$

We use a semi analytical Green's function approach (Geertsma, 1973; Kuvshinov, 2008) to relate compaction and displacement/stress. For details on the functions, the spatial smoothing used and the details on the stress calculation, see (Geertsma, 1973; Kuvshinov, 2008; Smith et al., 2022); and Supplementary Item 2.2. From the changes in shear stress, $\Delta\tau$, and effective normal stress ($\Delta\sigma'_{\mathrm{N}} = \Delta\sigma_{\mathrm{N}} - \Delta \mathrm{p}$), we compute the changes in Coulomb stress, $\Delta \mathrm{S}(\mathrm{x}, \mathrm{y}, \mathrm{t})$, computed 10 m above the reservoir and cumulated since 1960 (Figure.2A), using a positive sign for compressive stress as $\Delta \mathrm{S} = \Delta\tau + \mathrm{f}. \Delta\sigma'_{\mathrm{N}}$, with f the static friction coefficient of the rock. In

this field, the fault's dips are usually ~85º and the strikes show two dominant modes at N270◦ E and N350◦ E ((Smith et al., 2022); Figure.1A). We use the maximum Coulomb stress changes for both dominant receiver fault strike modes but results show little sensitivity to this choice (Smith et al., 2022), the chosen depth for calculation, and to f.

Our model is computationally efficient and consistent with the 3-D stress changes computed using other methods (Bourne et al., 2018; Buijze et al., 2017; Candela et al., 2019; Dahm & Hainzl, 2022; Dempsey & Suckale, 2017; Kühn et al., 2022; Van Wees et al., 2017). For detailed analysis of the effect of the different parameters of the model on seismicity forecasts, see Smith et al. (2022).

2.2.3 From stress changes to seismicity rate changes

Finally, we relate ΔS to the time-dependent seismicity rate change ΔR using the Threshold Rate and State failure function (TRS) of Heimisson et al. (Heimisson et al., 2022) which follows Dieterich's hypothesis (Dieterich, 1994) that earthquake nucleation is governed by rate and state friction but allows for a population of faults to be sub-critical initially (below steady-state), as expected in a quiet, intraplate tectonic context such as Groningen. A critical stress threshold (analog to the strength excess of the Coulomb Failure model) ΔS_c has to be overcome to reach self-sustained fault slip acceleration (earthquake nucleation) and produce seismicity Heimisson et al., 2022). The TRS model writes for every point in space (x, y):

$$\frac{\Delta R(t)}{r} = \frac{\exp\left(\frac{\Delta S(t) - \Delta S_c}{A\sigma_0}\right)}{\frac{1}{t_a}\int_{t_b}^{t} \exp\left(\frac{\Delta S(t') - \Delta S_c}{A\sigma_0}\right) dt' + 1} \quad \text{if } t \geq t_b, \text{ and} \tag{2}$$

$$\frac{\Delta R}{r} = 0$$

if $t \leq t_b$, with r the background seismicity rate (the seismicity rate that results from constant tectonic loading), $\Delta S(t)$ the change in Coulomb stress, ΔS_c the critical stress threshold, $A\sigma_0$ the frictional-stress parameter of Rate and State friction (Dieterich, 1994), t_a the characteristic time associated to the nucleation process characterizing the decay of seismicity to background rates after a stress step (Dieterich, 1994). Finally, t_b is the time at which ΔS first exceeded ΔS_c.

When the sources are critically stressed, $\Delta S_c \sim 0$, and the formulation (Eq.2) is equivalent to that of (Heimisson & Segall, 2018). The characteristic time, t_a relates to the secular background stressing rate, due to tectonic loading, $\dot{\tau}$, according to $t_a = \frac{A\sigma_0}{\dot{\tau}}$. It characterizes the nucleation process under such loading and would characterize the response time of the seismicity to a stress step added to the background seismicity. Note that if the system has been stressed, the relaxation time will change as described in section 3.2. The TRS formulation allows for earthquake nucleation to be time dependent and nucleation would be nearly instantaneous in the limit where its response time goes to zero, as is assumed in the standard Coulomb failure model which is also commonly used to relate stress changes to seismicity (*e.g.*, Dempsey & Suckale, 2017).

We sample a probability distribution of the TRS model parameters using an ensemble Markov Chain Monte Carlo ($MCMC$) algorithm (Foreman-Mackey et al., 2013) implemented in PyMC3 (Salvatier et al., 2016) with uniform priors and a non-local Poisson log-likelihood function (See supplementary Item 2.3). For all models generated in this study, we discretize the stress changes on a monthly basis to avoid numerical integration problems when comparing monthly and yearly discretizations. The difference between the 'monthly' and 'yearly' model inversions presented hereafter is that the input stress changes and seismicity for the 'yearly' models are smoothened using a 12-month average for the whole time-history. The posterior parameter space accounts therefore for epistemic uncertainty on the model's parameters. For both model types, we report the 1000 model parameter sets with the lowest negative log-likelihood to compare the information contained in the inversions. Additional details are given in Supplementary Item 2.3. Then, from the inverted model parameters we can generate the seismicity rates for the whole reservoir as function of time, $R(t)$. Finally, to generate earthquake catalogs we need to account for the aleatoric variability around the predicted rates which accounts for the fact that the earthquake generation is a non-stationary Poisson process of known rate. Details on the synthetic catalog generation are given in Supplementary Item 3.

2.2 Testing seasonality through the Schuster test & spectrum.

We test possible seasonality (periodicities) in the observed and synthetic seismicity catalogs using the Schuster test (Ader & Avouac, 2013; Beeler & Lockner, 2003; Schuster, 1897). For a tested period T, a phase θ_i is associated to each event i occurring at time t_i such that $\theta_i = 2\pi\frac{t_i}{T}$. Then, a 2D walk of N successive unit length steps in the phase direction are performed. The total distance D between the start and end points of the walk relates to the Schuster p-value which measures the probability that the walked length is the result of a random Poisson point process as $p = e^{-\frac{D^2}{N}}$, with N the total number of steps taken. Thus, the lower this $p-value$, the higher the probability that the detected periodicity is real. To study the correlation with a periodic perturbation, we evaluate the $p-value$ over a continuous range of periods $T \in [T_0, T_1]$ e.g. evaluating the Schuster spectrum (Ader & Avouac, 2013). The measured p-values can then be compared with the expected value, which depends on the tested period, not to be exceeded at a certain confidence level. The spectrum allows for identification of periodicities that have little probability to be due to chance because periodicities in the earthquake catalog will show as isolated low p-values in the spectrum, and event clusters will show as a drifting low p-value close to the characteristic time of the cluster (Ader & Avouac, 2013).

We define a new metric to characterize the capacity of the TRS models to capture seasonality as the vector distance error of the median of all synthetic catalog's Schuster random walks to that of the observed catalog. To separate their contribution, we also compute the phase, and distance errors for the median of all synthetic catalogs to the observed catalog. See Supplementary Item 4 for details.

3 Results and discussion

3.1 TRS model parameters not accounting for seasonal stress changes: 'yearly' models.

When seasonal fluctuations of ΔS and seismicity are ignored (Figure.1D, light purple curve), we obtain a 'yearly' TRS model which fits well the temporal (Figure.2A, green curve) and spatial distributions (Figure.2C) of seismicity. The prediction of the maximum-a-posteriori (MAP) yearly TRS model at the annual time scale is satisfying. However, if a range of acceptable models is considered (1000 best models out of 50,000, accounting for epistemic uncertainty), they yield widely different predictions outside the training period due to large trade-offs among the model parameters, especially between t_a and r (Figure.S3). The response time of seismicity to sub-annual stress variations is not well constrained in this inversion. To illustrate this effect, the green curves in Figure.2B show the response of the 1000 best yearly TRS models assuming no stress-changes after 2012 (frozen to $\Delta S(t_s)$, mimicking a hypothetical 'shut-in' at time t_s). The relaxation following the 'shut-in' is not characterized by t_a, (10-10,000 years for yearly TRS models), but by a new "accelerated" response time t_{acc} such that equation (2) becomes:

$$\frac{\Delta R}{r} = \frac{\exp\left(\frac{\Delta S(t_s) - \Delta S_c}{A\sigma_0}\right)}{1 + \frac{1}{t_a}\int_{t_b}^{t_s} \exp\left(\frac{\Delta S(t') - \Delta S_c}{A\sigma_0}\right) dt' + (t - t_s)\left(\frac{\exp\left(\frac{\Delta S(t_s) - \Delta S_c}{A\sigma_0}\right)}{t_a}\right)}$$

$$\frac{\Delta R}{r} = \frac{t_a}{(t - t_s) + \frac{t_a + \int_{t_b}^{t_s} \exp\left(\frac{\Delta S(t') - \Delta S_c}{A\sigma_0}\right) dt'}{\exp\left(\frac{\Delta S(t_s) - \Delta S_c}{A\sigma_0}\right)}} \quad (3)$$

We can identify this to the form:

$$\frac{\Delta R(t)}{r} = \frac{t_a}{(t - t_s) + t^{acc}}$$

whose characteristic decay time is:

$$t_a^{acc} = \frac{(t_a + \int_{t_b}^{t_s} \exp\left(\frac{\Delta S(t') - \Delta S_c}{A\sigma_0}\right) dt')}{\exp\left(\frac{\Delta S(t_s) - \Delta S_c}{A\sigma_0}\right)} \quad (4)$$

t_a^{acc} becomes much shorter than t_a because the nucleation process is accelerated exponentially due to stress increase induced by the reservoir compaction. Assuming an approximately linear increase of $\Delta S(t)$ at the multiannual time scale, it converges quickly toward $t_a^{acc}(t_s) \sim \frac{A\sigma_0 \cdot \Delta t}{\Delta S(t_s)}$ where Δt is the duration of production from onset of seismicity to "shut in". It is therefore inversely proportional to the average stressing rate, $\frac{\Delta S(t_s)}{\Delta t}$, and proportional to $A\sigma_0$. In effect, our best yearly TRS models show t_a^{acc} ranging from 0.1 to 200 years after a hypothetical shut-in, showing that $A\sigma_0$ is poorly constrained (Figure.S4, green curves, Figure.S3A).

3.2 Seasonal stress changes effect on model parameter inversion: 'monthly' models.

We next take seasonal stress variations into account (Figure.3, Figure.1B,D). At the sub-yearly timescale, pressure is not homogenized over the whole reservoir. Given the permeability (k~3.55e-13 m^2) and porosity (ϕ~15%) of the reservoir, its average hydraulic diffusivity is α_{hy}~0.5 m^2/s and its characteristic diffusion length over one year is $r_{hy} = \sqrt{2\pi\alpha_{hy}t}$ ~10 km

which is smaller than the minimum length scale from any well cluster to the reservoir's edge (Figure.1B), effectively resulting in smeared seasonal reservoir pressure. This damping effect and the heterogeneity in reservoir compressibility (Burkitov et al., 2016; Smith et al., 2019) control the spatial distribution of seasonal ΔS amplitude (Figure.3D) which can reach ~20 kPa (Figure.3A, B). The effect of seasonal stress variations could be significant if the seismicity response to stress changes is fast enough. Figure.3E compares the observed seasonal variation of seismicity rate, obtained by stacking monthly rates for all years between 1991 and 2014 (orange curve), with the seasonal variation expected for the CF model with instantaneous nucleation (Figure.3E, yellow curve). In that case, since the stress evolution is monotonic, the seismicity rate is proportional to the Coulomb stress rate, $\Delta\dot{S}$ (Ader & Avouac, 2013; Dempsey & Suckale, 2023). The observed seasonal variation is much smaller than predicted by the instantaneous nucleation model and is out of phase by about 3 months. A time dependent nucleation process can in principle explain both the phase shift and the damped response (Ader & Avouac, 2013) as explored next.

We construct a 'monthly' TRS model which accounts for seasonal stress variations. The stress changes are computed using monthly gas extractions (Figure.3, Figure.1D, blue curve). The 'monthly' and 'yearly' TRS models predict temporal (Figure.2A) and spatial (Figure.2C,D) distributions of seismicity that fit equally well the observations (Figure.2E) but yield significantly different posterior model parameter distributions (Figure.S3). When seasonality in ΔS is accounted for, both the product $r.t_a$ and $A\sigma_0$ are tightly constrained (Figure. S3, blue points). The available seismic catalog is insufficient to derive good constraints on the background seismicity rate so the trade-off between t_a and r cannot be resolved, but the performance of the forecast is good as it depends chiefly on $r.t_a$ and $A\sigma_0$ which are relatively well constrained. Better constraints in the 'monthly' TRS model parameters lead to consistently shorter and more tightly constrained relaxation times in response to changes in ΔS (Figure.2B, Figure.S4).

3.3 Constraining the nucleation characteristics from earthquake seasonality.

We now assess the ability of the TRS models to explain both the phase and amplitude of the seismicity response to seasonal stress variations. We adopt the Schuster test & spectrum ((Ader & Avouac, 2013), Supplementary Item 3) which allows searching for any possible periodicity by building a spectrum of the Schuster p-values (Ader & Avouac, 2013; Chanard et al., 2019). The Schuster spectrum calculated on the 1991-2022 Groningen earthquake catalog (Dost et al., 2017; KNMI, 2023) for $M \geq 1.1$, shows a significant, isolated periodicity at 1-year period (Figure.4, orange colors, Figure.S6). The Schuster p-value at 1 year (~2.4e-3) uniquely falls above 90% confidence level (meaning the chance of one tested period yielding such a low p-value being due to chance is less than 10%). The corresponding Schuster walk at 1-year (Figure.4, orange wiggles, (Beeler & Lockner, 2003; Noël et al., 2019)) shows consistent year to year drift indicative of excess seismicity in the winter, peaking between March and April, delayed with respect to peak extraction rates in January but synchronized with the maximum amplitude of calculated pressure, and ΔS in most of the reservoir (Figure.3D, and orange tick in Figure.4C,D). Note that if smaller earthquakes were considered in the analysis, the seasonality amplitude would become larger (Figure.S6). The Schuster test and spectrum are not affected by the use of different magnitudes of completion, but we keep only events with magnitude ≥ 1.1 for consistency with the presented earthquake forecasts. To test if the observed seasonality is predicted by TRS models, we generate 100 synthetic catalogs from the MAP TRS models

accounting for aleatoric variability in the seismicity generation (Figure.S5) and calculate a Schuster spectrum (Figure.4A,B) and a Schuster walk at 1 year period (Figure.4C, D) for each catalog. The catalogs generated with the monthly TRS model (accounting for seasonal stress variations in the model inference and forecast) show clear periodicity at 1-year period with p-values centered around the observed catalog ones, quantitatively recovering the amplitude of seasonality (Figure.4A, blue dots). Remarkably, the synthetic catalogs generated from the MAP 'monthly' TRS model (Figure.4C, blue wiggles) show a marked drift, with similar phase and amplitude as the observed catalog. We also generate synthetic catalogs using the MAP parameters of the 'yearly' TRS model but using the seasonal variation of ΔS in input (Figure.4B, D, green colors). These example catalogs show no significant periodicity above ~50% confidence. This 'yearly' model predicts a more damped response to temporal variations of seasonal stress changes. We statistically quantify the capacity of the models to constrain annual seasonal variations though the errors of the Schuster walks at 1 year period on synthetic catalogs (aleatoric uncertainty) with seasonal stress input to the observed walk (Figure.4F, Figure.S7). Remarkably, the 1000 best models (epistemic uncertainty) using yearly TRS models show ~one order of magnitude larger errors in phase and amplitude of seasonality compared to the monthly TRS ones (Figure.4F). Using this seasonal analysis and the metrics to quantify seasonality, we can further tighten the constraints on the range of admissible parameters (Figure.4E, Figure.S3B light blue dots). Finally, we evaluate the seasonality predicted by the instantaneous nucleation CF model in Figure.4E (yellow curves). This model strongly over-predicts seasonality and responds in phase to the maximum Coulomb stress rate, $\dot{\Delta S}$, (Ader & Avouac, 2013; Dempsey & Suckale, 2023), effectively showing that the nucleation process cannot be instantaneous.

Solid Earth tides -deformations of Earth's surface caused by gravitational forces- are another source of short-timescale stress variations that may also affect seismicity (Cochran et al., 2004). In Groningen, the amplitude of stress variations due to tidal loads is <0.5 kPa (Figure.S8, Supplementary Text) so ~40 times smaller than the estimated amplitude due to seasonal extraction variations, consistently with the observation that the Schuster spectrum doesn't reveal any detectable periodicity at the dominant semi-diurnal and diurnal tidal periods (Figure.S6).

4 Conclusions and implications

Our results highlight the merit of accounting for the finite duration of earthquake nucleation and a possible initial strength excess to forecast induced seismicity. These two elements are needed to obtain a model that can predict the response of seismicity to stress changes on both short and long timescales, and we have proposed a method to quantify the goodness of fit to the short-timescales in addition to the conventional evaluation on long timescales. If the initial strength excess is ignored (Candela et al., 2019), the seismicity response time can be overestimated by orders of magnitude leading to seismicity forecasts with a sustained seismicity tail because the delay between the start of operations and the onset of seismicity is adsorbed by a long characteristic nucleation time (Candela et al., 2019). This bias effectively shuts-down the effect of short-timescale stress variations, and over-predicts seismicity rates following decreases in fluid extraction rates (Figure.2B, (Heimisson et al., 2022)). Alternative formulations than rate-and-state friction to account for a finite nucleation time (Dahm & Hainzl, 2022; Zhai et al., 2019) should lead to a similar behavior.

The mitigation of seismic hazard associated to subsurface fluid injection or extraction operations may be improved by accelerating model calibrations in three ways. First, the deployment of a sensitive seismic network well before starting subsurface operations, combined

with enhanced earthquake detection techniques (Kong et al., 2018) would help constrain the background seismicity rates (r, which presents a strong tradeoff with t_a, Figure.S3) and reveal any induced seismicity early on, allowing for early calibration of the forecasting model. Second, varying fluid injection or production rates in a harmonic manner with various periods, would also help tighten the forecasting model (even if no correlated seismicity response is observed). Third, by performing shut-in operations over long enough time durations to track and constrain the relaxation of seismicity. Unbiased forecasting models of induced seismicity obtained by coupling pressure modelling with geomechanical deformation and seismicity should help mitigate the risk associated to the exploitation of subsurface reservoirs (geothermal, CO2 sequestration, hydrogen storage, hydrocarbon extraction).

Finally, stress variations at short and long times scales also affect natural systems (tectonic loading, post-seismic relaxation, hydrological/glacial load variations, and fault-to-fault interactions) and their seismicity response can provide insight into earthquake physics as shown here for induced seismicity. Commonly, in such studies, only one source of stress variations is considered, and our study shows that using a model calibrated at one time scale to forecast seismicity at another time scale can be flawed.

Acknowledgments

This study was supported by the NSF/IUCRC Geomechanics and Mitigation of Geohazards (National Science Foundation award # 1822214), and Extended Project GMG-3. M.A. Acknowledges funding from the Swiss National Science Foundation through grant P2ELP2_195127. We gratefully acknowledge data and support from Shell Global Solutions. Authors declare that they have no competing interests.

Open Research

The data needed to reproduce this article can be found in (Burkitov et al., 2016; Oates et al., 2022). Codes necessary for the reproduction of figures in this article are available through ref (Acosta et al., 2023).

References

Acosta, M., Avouac, J.-P., Smith, J. D., Sirorattanakul, K., Kaveh, H., & Bourne, S. J. (2023). Dataset and codes for : Earthquake nucleation characteristics revealed by seismicity response to seasonal stress variations induced by gas production at Groningen. https://doi.org/10.5281/zenodo.8140825

Ader, T. J., & Avouac, J.-P. (2013). Detecting periodicities and declustering in earthquake catalogs using the Schuster spectrum, application to Himalayan seismicity. *Earth and Planetary Science Letters*, *377–378*, 97–105. https://doi.org/10.1016/j.epsl.2013.06.032

Ader, T. J., Lapusta, N., Avouac, J. P., & Ampuero, J. P. (2014). Response of rate-and-state seismogenic faults to harmonic shear-stress perturbations. *Geophysical Journal International*, *198*(1), 385–413. https://doi.org/10.1093/gji/ggu144

Beeler, N., & Lockner, D. (2003). Why earthquakes correlate weakly with the solid Earth tides: Effects of periodic stress on the rate and probability of earthquake occurrence. *Journal of Geophysical Research*, *https://doi.org/10.1029/2001JB001518*.

Bourne, S. J., & Oates, S. J. (2017a). Development of statistical geomechanical models for forecasting seismicity induced by gas production from the Groningen field. *Geologie En Mijnbouw/Netherlands Journal of Geosciences*, *96*(5), s175–s182. https://doi.org/10.1017/njg.2017.35

Bourne, S. J., & Oates, S. J. (2017b). Extreme Threshold Failures Within a Heterogeneous Elastic Thin Sheet and the Spatial-Temporal Development of Induced Seismicity Within the Groningen Gas Field. *Journal of Geophysical Research: Solid Earth*, *122*(12), 10,299-10,320. https://doi.org/10.1002/2017JB014356

Bourne, S. J., Oates, S., van Elk, J., & Doornhof, D. (2014). A seismological model for earthquakes induced by fluid extraction from a subsurface reservoir. *Journal of Geophysical Research: Solid Earth*, *119*, 8991–9015.

Bourne, S. J., Oates, S. J., & van Elk, J. (2018). The exponential rise of induced seismicity with increasing stress levels in the Groningen gas field and its implications for controlling seismic risk. *Geophysical Journal International*, *213*(3), 1693–1700. https://doi.org/10.1093/gji/ggy084

Buijze, L., van den Bogert, P., Wassing, B., Orlic, B., & ten Veen, J. (2017). Fault reactivation mechanisms and dynmanic rupture modelling of depletion-induced seismic events in a

{R}otliegend gas reservoir. *Netherlands Journal of Geosciences*, *https://doi.org/10.1017/njg.2017.27*.

Burkitov et al., P. (2016). Groningen Field Review 2015 Subsurface Dynamic Modelling Report. *Nederlandse Aardolie Maatschappij*, 131. https://nam-feitenencijfers.data-app.nl/download/rapport/e683753a-e085-417d-995d-b7ae7a9c820f?open=true

Candela, T., Wassing, B., ter Heege, J., & Buijze, L. (2018). How earthquakes are induced. *Science*, *360*(6389), 598–600. https://doi.org/10.1126/science.aat2776

Candela, T., Osinga, S., Ampuero, J.-P., Wassing, B., Pluymaekers, M., Fokker, P. A., et al. (2019). Depletion-Induced Seismicity at the Groningen Gas Field: Coulomb Rate-and-State Models Including Differential Compaction Effect. *Journal of Geophysical Research: Solid Earth*, *124*(7), 7081–7104. https://doi.org/10.1029/2018JB016670

Chanard, K., Nicolas, A., Hatano, T., Petrelis, F., Latour, S., Vinciguerra, S., & Schubnel, A. (2019). Sensitivity of Acoustic Emission Triggering to Small Pore Pressure Cycling Perturbations During Brittle Creep. *Geophysical Research Letters*, *46*(13), 7414–7423. https://doi.org/10.1029/2019GL082093

Cochran, E. S., Vidale, J. E., & Tanaka, S. (2004). Earth Tides Can Trigger Shallow Thrust Fault Earthquakes. *Science*, *306*(5699), 1164–1166. https://doi.org/10.1126/science.1103961

Dahm, T., & Hainzl, S. (2022). A Coulomb Stress Response Model for Time-Dependent Earthquake Forecasts. *Journal of Geophysical Research: Solid Earth*, *127*(9). https://doi.org/10.1029/2022JB024443

Dempsey, D., & Suckale, J. (2017). Physics-based forecasting of induced seismicity at {G}roningen gas field, the {N}etherlands. *Geophysical Research Letters*, *44*, 7773–7782.

Dempsey, D., & Suckale, J. (2023). Physics-Based Forecasting of Induced Seismicity at Groningen Gas Field, The Netherlands: Post Hoc Evaluation and Forecast Update. *Seismological Research Letters*, *94*(3), 1429–1446. https://doi.org/10.1785/0220220317

Dieterich, J. (1994). A constitutive law for rate of earthquake production and its application to earthquake clustering. *Journal of Geophysical Research*, *https://doi.org/10.1029/93JB02581*.

Dost, B., & Kraaijpoel, D. (2013). The August 16, 2012 earthquake near Huizinge (Groningen). De Bilt, The Netherlands: Koninklijk Nederlands Meteorologisch Instituut.

Dost, B., Ruigrok, E., & Spetzler, J. (2017). Development of seismicity and probabilistic hazard assessment for the Groningen gas field. *Netherlands Journal of Geosciences*, *96*(5), s235–s245. https://doi.org/10.1017/njg.2017.20

Ellsworth, W. L. (2013). Injection-Induced Earthquakes. *Science*, *341*(6142), 1225942–1225942. https://doi.org/10.1126/science.1225942

Foreman-Mackey, D., Hogg, D. W., Lang, D., & Goodman, J. (2013). emcee: The MCMC Hammer. *Publications of the Astronomical Society of the Pacific*, *125*(925), 306. https://doi.org/10.1086/670067

Geertsma, J. (1973). Land Subsidence Above Compacting Oil and Gas Reservoirs. *Journal of Petroleum Technology*, *25*(06), 734–744. https://doi.org/10.2118/3730-PA

Goebel, T. H. W., & Brodsky, E. E. (2018). The spatial footprint of injection wells in a global compilation of induced earthquake sequences. *Science*. https://doi.org/10.1126/science.aat5449

Grigoli, F., Cesca, S., Priolo, E., Rinaldi, A. P., Clinton, J. F., Stabile, T. A., et al. (2017). Current challenges in monitoring, discrimination, and management of induced seismicity

related to underground industrial activities: A European perspective. *Reviews of Geophysics*, *55*(2), 310–340. https://doi.org/10.1002/2016RG000542

Heimisson, E. R., & Segall, P. (2018). Constitutive Law for Earthquake Production Based on Rate-and-State Friction: Dieterich 1994 Revisited. *Journal of Geophysical Research: Solid Earth*, *123*(5), 4141–4156. https://doi.org/10.1029/2018JB015656

Heimisson, E. R., Smith, J. D., Avouac, J.-P., & Bourne, S. J. (2022). Coulomb Threshold Rate-and-State Model for Fault Reactivation: Application to induced seismicity at Groningen, *228*(3), 2061–2072. https://doi.org/10.1093/gji/ggab467

Heimisson, R., Smith, J. D., Avouac, J., & Bourne, S. J. (2021). Coulomb Threshold Rate-and-State Model for Fault Reactivation : Application to induced seismicity at Groningen.

de Jager, J., & Visser, C. (2017). Geology of the Groningen field – an overview. *Netherlands Journal of Geosciences*, *96*(5), s3–s15. https://doi.org/10.1017/njg.2017.22

Kaiser, J. (1950). *Untersuchungen über das Auftreten von Geräuschen beim Zugversuch* (PhD Thesis). Der Technischen Hochschule München.

Kaven, J., Hickman, S., McGarr, A., & Ellsworth, W. (2015). Surface monitoring of microseismicity at the {D}ecatur, {I}llinois, \ce{CO2} sequestration demonstration site. *Seismological Research Letters*, *86*, 1096–1101.

King, G., Stein, R., & Lin, J. (1994). Static stress changes and the triggering of earthquakes. *Bulletin of the Seismological Society of America*, *84*, 935–953.

KNMI. (2023). KNMI Earthquake Catalog - Groningen - Last Accessed 2023.01.25 [Data set]. Retrieved from https://dataplatform.knmi.nl/dataset/aardbevingen-cijfers-1

Kong, Q., Trugman, D. T., Ross, Z. E., Bianco, M. J., Meade, B. J., & Gerstoft, P. (2018). Machine Learning in Seismology: Turning Data into Insights. *Seismological Research Letters*, *90*(1), 3–14. https://doi.org/10.1785/0220180259

Kühn, D., Hainzl, S., Dahm, T., Richter, G., & Vera Rodriguez, I. (2022). A review of source models to further the understanding of the seismicity of the Groningen field. *Netherlands Journal of Geosciences*, *101*, e11. https://doi.org/10.1017/njg.2022.7

Kuvshinov, B. N. (2008). Elastic and piezoelectric fields due to polyhedral inclusions. *International Journal of Solids and Structures*, *45*(5), 1352–1384. https://doi.org/10.1016/j.ijsolstr.2007.09.024

Langenbruch, C., Weingarten, M., & Zoback, M. D. (2018). Physics-based forecasting of man-made earthquake hazards in Oklahoma and Kansas. *Nature Communications*, *9*(1), 3946. https://doi.org/10.1038/s41467-018-06167-4

Logg, A., Mardal, K.-A., & Wells, G. (2012). *Automated Solution of Differential Equations by the Finite Element Method The FEniCS book.* (Vol. Vol. 84.). Springer Science & Business Media. Retrieved from https://link.springer.com/book/10.1007/978-3-642-23099-8

Meyer, H., Smith, J. D., Bourne, S. J., & Avouac, J.-P. (2022). An integrated framework for surface deformation modeling and induced seismicity forecasting due to reservoir operations. *Geological Society, London, Special Publications*, *528*(1), SP528-2022–169. https://doi.org/10.1144/SP528-2022-169

Noël, C., Passelègue, F. X., Giorgetti, C., & Violay, M. (2019). Fault Reactivation During Fluid Pressure Oscillations: Transition From Stable to Unstable Slip. *Journal of Geophysical Research: Solid Earth*, *124*(11), 10940–10953. https://doi.org/10.1029/2019JB018517

494 Oates, S., Landman, A. J., van der Wal, O., Baehr, H., & Piening, H. (2022, September 23).
495 Geomechanical, seismological, and geodetic data pertaining to the Groningen gas field: a
496 data package used in the "Mmax II Workshop", on constraining the maximum earthquake
497 magnitude in the Groningen field [Datapackage]. https://doi.org/10.24416/UU01-
498 RHHRPY
499 Post, R. A. J., Michels, M. A. J., Ampuero, J.-P., Candela, T., Fokker, P. A., van Wees, J.-D., et
500 al. (2021). Interevent-time distribution and aftershock frequency in non-stationary
501 induced seismicity. *Scientific Reports*, *11*(1), 3540. https://doi.org/10.1038/s41598-021-
502 82803-2
503 Raleigh, C., Healy, J., & Bredehoeft, J. (1976). An experiment in earthquake control at Rangely,
504 Colorado. *Science*.
505 Richter, G., Hainzl, S., Dahm, T., & Zöller, G. (2020). Stress-based, statistical modeling of the
506 induced seismicity at the Groningen gas field, The Netherlands. *Environmental Earth*
507 *Sciences*, *79*(11), 252. https://doi.org/10.1007/s12665-020-08941-4
508 Salvatier, J., Wiecki, T. V., & Fonnesbeck, C. (2016). Probabilistic programming in Python
509 using PyMC3. *PeerJ Computer Science*, *2*, e55. https://doi.org/10.7717/peerj-cs.55
510 Scholz, C. H. (2019). *The Mechanics of Earthquakes and Faulting* (3rd ed.). Cambridge:
511 Cambridge University Press. https://doi.org/10.1017/9781316681473
512 Schuster. (1897). On lunar and solar periodicities of earthquakes |. *Proceedings of the Royal*
513 *Society of London.* Retrieved from
514 https://royalsocietypublishing.org/doi/10.1098/rspl.1897.0060

Shirzaei, M., Ellsworth, W. L., Tiampo, K. F., González, P. J., & Manga, M. (2016). Surface uplift and time-dependent seismic hazard due to fluid injection in eastern Texas. *Science*, *353*(6306), 1416–1419. https://doi.org/10.1126/science.aag0262

Smith, J. D., Avouac, J. P., White, R. S., Copley, A., Gualandi, A., & Bourne, S. J. (2019). Reconciling the Long-Term Relationship Between Reservoir Pore Pressure Depletion and Compaction in the Groningen Region. *Journal of Geophysical Research: Solid Earth*, *124*(6), 6165–6178. https://doi.org/10.1029/2018JB016801

Smith, J. D., White, R. S., Avouac, J. P., & Bourne, S. J. (2020). Probabilistic earthquake locations of induced seismicity in the Groningen region, the Netherlands. *Geophysical Journal International*, *222*(1), 507–516. https://doi.org/10.1093/GJI/GGAA179

Smith, J. D., Heimison, Elias R, Bourne, S. J., & Avouac, Jean-Philippe. (2022). Stress-based forecasting of induced seismicity with instantaneous earthquake failure functions : Applications to the Groningen Gas Reservoir . *Earth and Planetary Science Letters*, *594*. https://doi.org/10.1016/j.epsl.2022.117697.

Supplementary Materials and Methods. (n.d.).

van Thienen-Visser, K., & Breunese, J. (2015). Induced seismicity of the {G}roningen gas field: {H}istory and recent developments. *The Leading Edge*, *34*, 664–671.

Trampert, J., Benzi, R., & Toschi, F. (2022). Implications of the statistics of seismicity recorded within the Groningen gas field. *Netherlands Journal of Geosciences*, *101*, e9. https://doi.org/10.1017/njg.2022.8

Van Wees, J.-D., Fokker, P. A., Van Thienen-Visser, K., Wassing, B. B. T., Osinga, S., Orlic, B., et al. (2017). Geomechanical models for induced seismicity in the Netherlands: inferences from simplified analytical, finite element and rupture model approaches.

Netherlands Journal of Geosciences, *96*(5), s183–s202. https://doi.org/10.1017/njg.2017.38

Walsh, F., & Zoback, M. (2015). Oklahoma's recent earthquakes and saltwater disposal. *Science Advances*, *1*.

Willacy, C., van Dedem, E., Minisini, S., Li, J., Blokland, J. W., Das, I., & Droujinine, A. (2018). Application of full-waveform event location and moment-tensor inversion for Groningen induced seismicity. *The Leading Edge*, *37*(2), 92–99. https://doi.org/10.1190/tle37020092.1

Zaliapin, I., & Ben-Zion, Y. (2013). Earthquake clusters in southern California I: Identification and stability: IDENTIFICATION OF EARTHQUAKE CLUSTERS. *Journal of Geophysical Research: Solid Earth*, *118*(6), 2847–2864. https://doi.org/10.1002/jgrb.50179

Zhai, G., Shirzaei, M., Manga, M., & Chen, X. (2019). Pore-pressure diffusion, enhanced by poroelastic stresses, controls induced seismicity in Oklahoma. *Proceedings of the National Academy of Sciences*, *116*(33), 16228–16233. https://doi.org/10.1073/pnas.1819225116

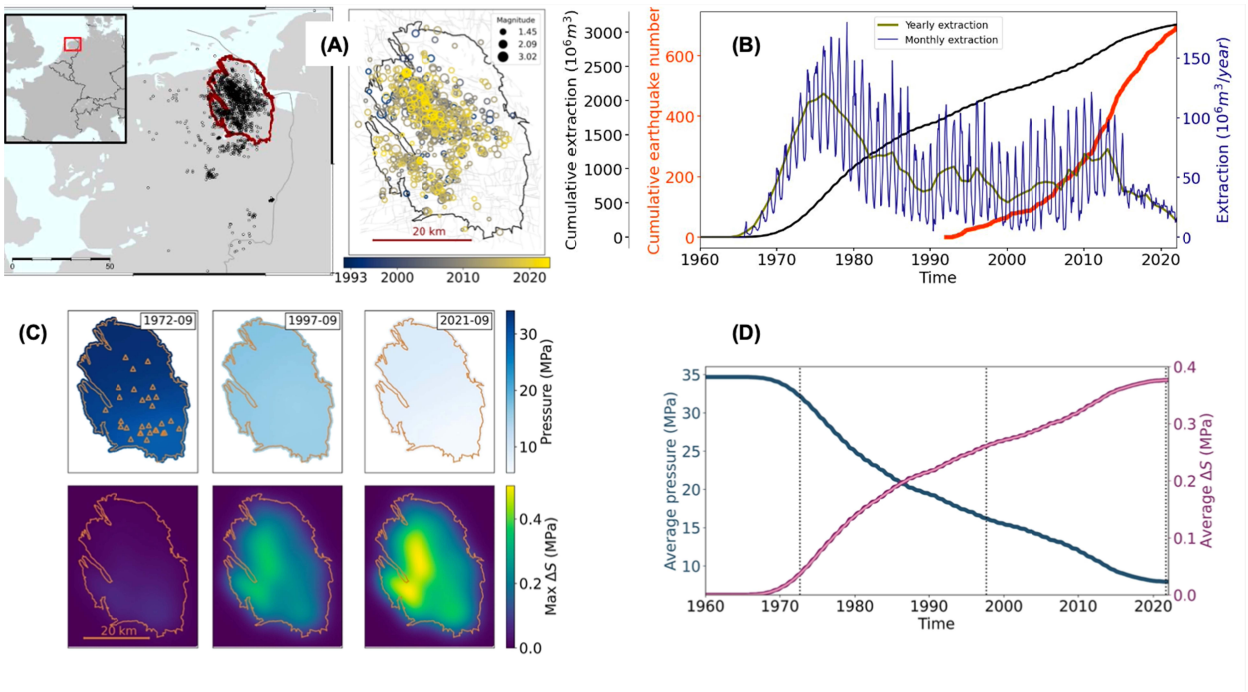

Figure. 1. The Groningen gas field & simulation results.
(A) Geographic context showing extensive seismicity due to the gas field in an otherwise stable tectonic setting (left), and top view of the reservoir (right) showing identified faults (gray traces (Oates et al., 2022)), and the earthquake catalog (with magnitude ≥1.1; (Dost et al., 2017; KNMI, 2023)) color coded by time. Sizes represent the earthquake magnitudes. **(B)** Observed data averaged over the gas reservoir versus time. Left y-axes show cumulative extraction (black), and cumulative earthquake number in orange since 1991, 34 years after the start of extraction. Right y-axis shows the discretized extraction data averaged either yearly (green line), or monthly (blue line). The monthly averaged extraction shows more than 80% seasonal variations with more gas extraction in the winter months. **(C)** Map view snapshots of simulation results at the dates shown in inset: fluid pressure (top row, with the position of extraction well clusters shown as triangles) and maximum Coulomb stress change calculated 10 m above the reservoir (ΔS, bottom row). **(D)** Simulation results averaged over the reservoir versus time. Left y-axis shows pressure (blue), and right y-axis shows maximum Coulomb stress changes (dark purple includes seasonal variations used as input for the monthly TRS model inversions, light purple shows smoothened seasonality used as input for the yearly TRS model inversions). Vertical dotted lines correspond to the snapshots shown in panel (C).

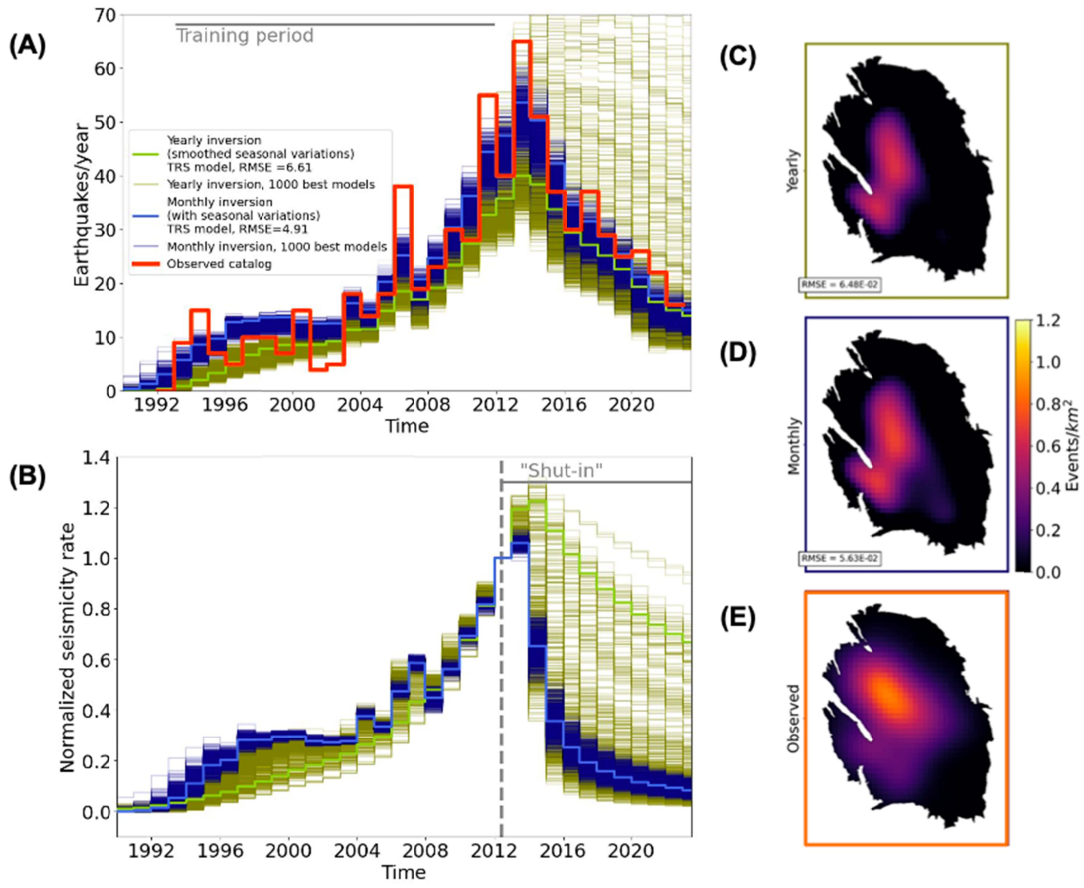

Figure. 2. Yearly averaged seismicity rate forecasts for different models. (A) Earthquake rates comparing observed seismicity (orange curve, for $M \geq 1.1$), and inversions for the different models tested in this study. Green curves represent the yearly inversion (seasonality smoothened out in input Coulomb stress). Blue curves represent the monthly inversion (seasonality accounted for in input Coulomb stress). Thin lines represent the 1000 best models out of 50 000, accounting for epistemic uncertainty on model parameters. Thick lighter lines show the Maximum-A-Posteriori models from MCMC inversion. Gray line represents the training period from 1993 to 2012. **(B)** Predicted seismicity rates for a hypothetical 'shut-in' of the reservoir with no change of Coulomb stress past 2012 (dashed gray line). All curves are normalized to 2012. A Coulomb failure model with instantaneous nucleation would predict an immediate drop of the seismicity to the background level. Colors correspond to the inversions in (A), and different lines represent the 1000 best models. **(C, D, E)** Epicentral event density for the MAP models for yearly (C), monthly (D), and for the observed catalog (E).

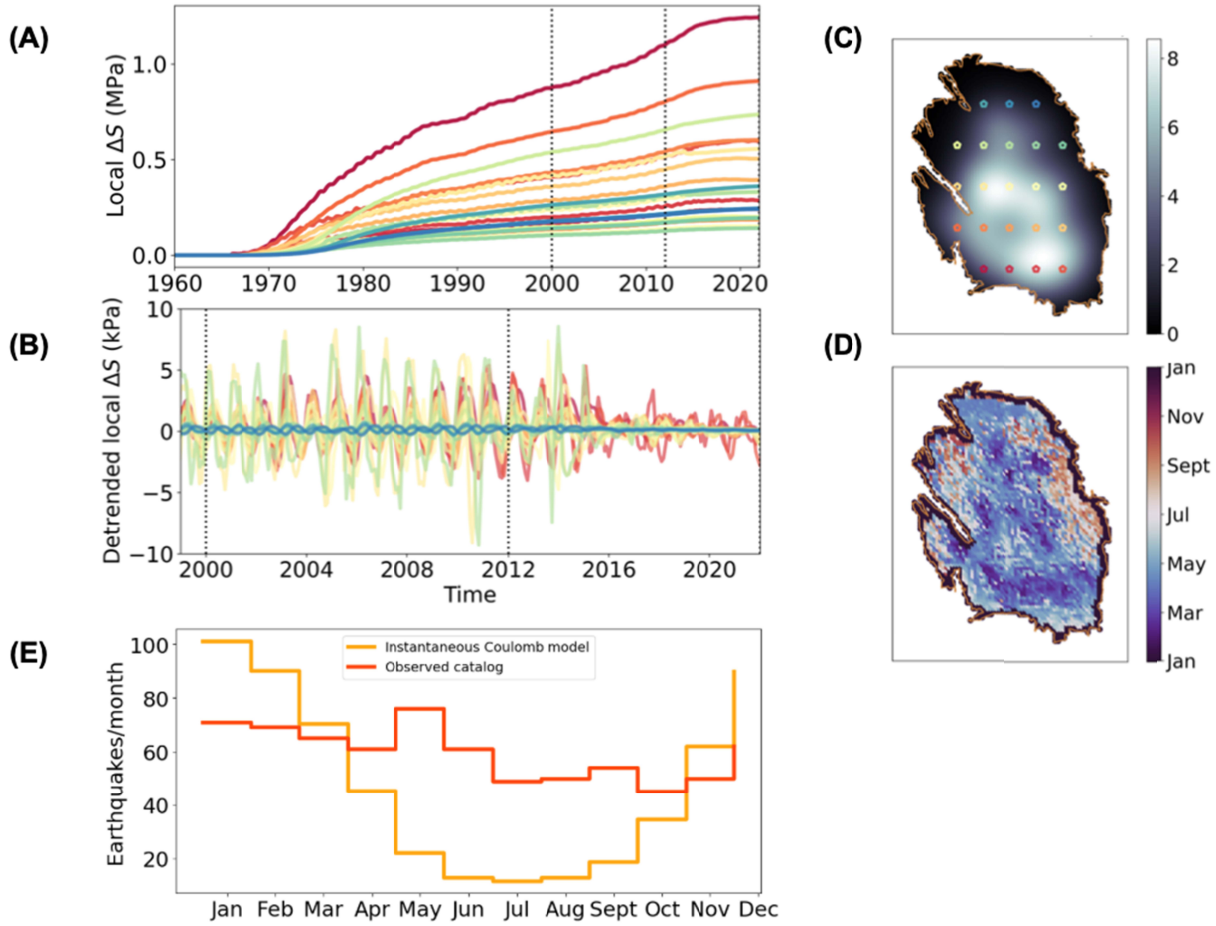

Figure. 3. Spatial and temporal seasonal stress variations in the field & stacked seismicity. **(A)** Simulated local stress changes versus time at discrete locations color-coded in panel (C). **(B)** 12-month moving average detrended local stress changes at the same locations as in panel (A) versus time for the 1999-2021 period. The seasonal amplitudes of extraction and thus of stress changes were drastically reduced following the M_w3.6 Huizinge earthquake. **(C)** Map view of maximum seasonal stress variations peak-to-peak amplitude between 2000 and 2012. The points color-code locations at which local Coulomb stress evolution in time is shown in panels (A) and (B). **(D)** Mean month (during the 2000 to 2012 period) where the local maximum seasonal stress variations occur in the reservoir. The edges of the reservoir show a clear phase change for occurrence of maximum seasonal stress variations but have small amplitudes whereas the central and southern regions of the reservoir have in-phase large seasonal stress amplitudes (e.g., panel C). **(E)** Seasonal variation of seismicity rate obtained by stacking all years between 1990 and 2021 in the observed catalog (orange curve) compared with prediction of a Coulomb failure model with instantaneous nucleation (yellow curve, seismicity rate proportional to stress rate).

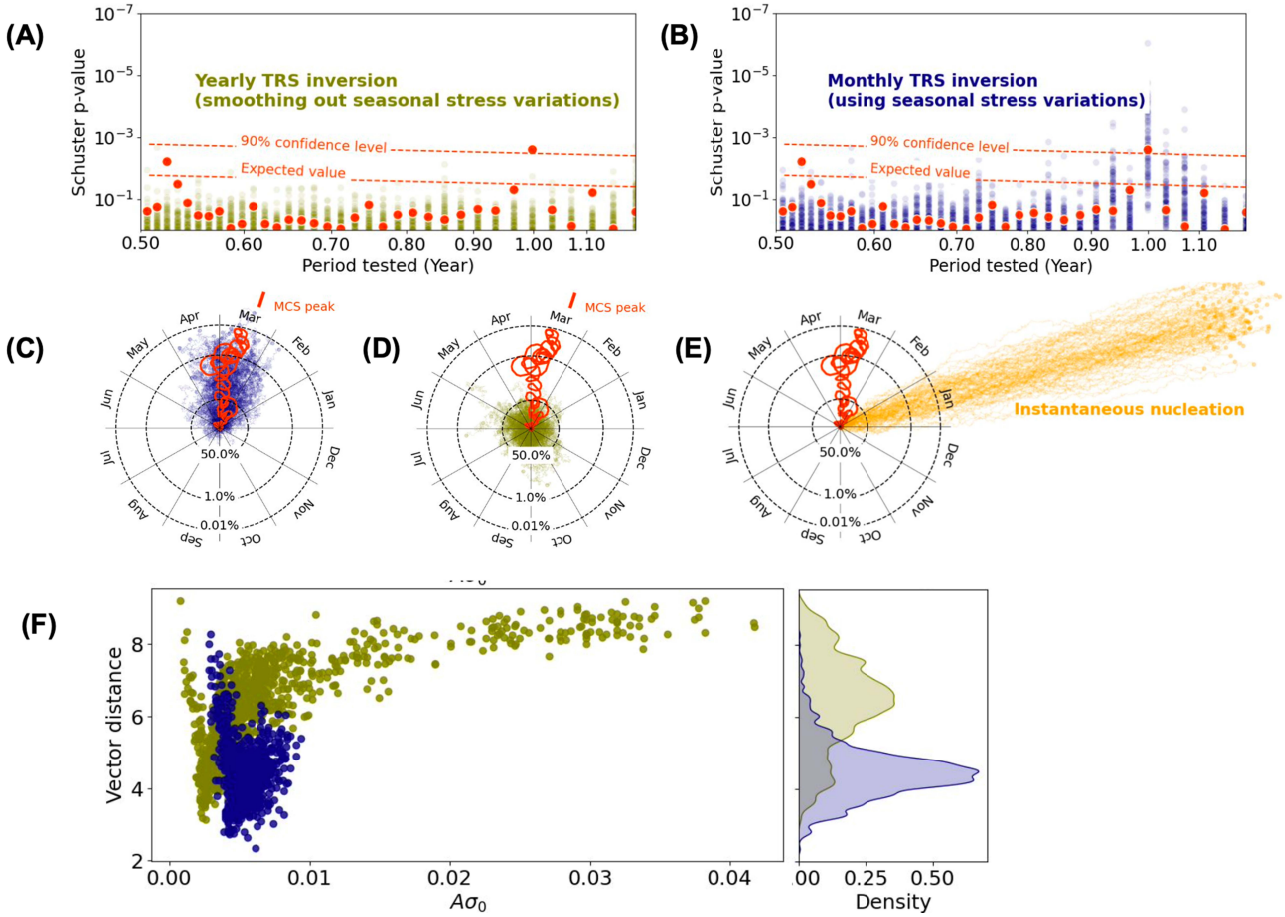

Figure. 4. Quantitative constraints on earthquake nucleation models using seasonality. (A, B) Schuster spectrum (Ader & Avouac, 2013) for the observed catalog (with $M \geq 1.1$, orange points), and 100 synthetic catalogs (accounting for aleatoric uncertainty, Supplementary Material, Figure.S5) derived from the yearly ((A), blue points), and monthly ((B), green points) MAP TRS models respectively. The Schuster spectrum is evaluated for periods from 6 to 18 months (a larger range of period spectra is shown in Figure.S6). Low, isolated p-values quantify seasonality at a given period. **(C, D, E)** Schuster random walks at 1 year period on the same catalogs as (A) and (B) respectively, and the instantaneous CF model (**(E),** orange lines). Circles denote the probability that the seismicity results from a random process at 50, 1, and 0.1% levels. Drift direction reflects the times of year with the maximum seismicity rate. The orange tick mark (MCS) shows the phase of the maximum seasonal Coulomb stress averaged over the whole reservoir history (March-April). The observed catalog (orange lines) shows a clear maximum in seismicity rate toward March-April. This phase (and amplitude) is quantitatively recovered by the shown monthly TRS model (considering seasonal stress variations in input). The example yearly TRS model does not show signs of seasonality. The instantaneous TRS model overestimates the seasonality. **(F)** Median vector distance error of synthetic catalogs to the observed catalog versus the parameter $A\sigma_0$ (Supplementary Material). The right-hand inset show the error density.